

New, late-type spectroscopic binaries with X-ray emission[★]

A. Frasca^{1†}, G. Catanzaro¹, I. Busà¹, P. Guillout², J. Alonso-Santiago¹, C. Ferrara^{3,1},
M. Giarrusso^{4,1}, M. Munari¹, F. Leone^{3,1}

¹INAF-Osservatorio Astrofisico di Catania, Via S.Sofia 78, I-95123, Catania, Italy

²Université de Strasbourg, CNRS, Observatoire Astronomique de Strasbourg, UMR 7550, F-67000 Strasbourg, France

³Università degli studi di Catania, Via S.Sofia 78, I-95123, Catania, Italy

⁴Università degli Studi di Firenze, Dipartimento di Fisica e Astronomia, Largo E. Fermi 2, I-50125 Firenze, Italy

Accepted 2022 June 30. Received 2022 June 24

ABSTRACT

In this paper we present a spectroscopic study of six double-lined binaries, five of which were recently discovered in a high-resolution spectroscopic survey of optical counterparts of stellar X-ray sources. Thanks to high-resolution spectra acquired with CAOS spectropolarimeter during seven years, we were able to measure the radial velocities of their components and determine their orbital elements. We have applied our code COMPO2 to determine the spectral types and atmospheric parameters of the components of these spectroscopic binaries and found that two of these systems are composed of main sequence stars, while the other four contain at least one evolved (giant or subgiant) component, similar to other well-known RS CVn systems. The subtraction of a photospheric template built up with spectra of non-active stars of the same spectral type as those of the components of each system has allowed us to investigate the chromospheric emission that fills in the H α cores. We found that the colder component is normally the one with the largest H α emission. None of the systems show a detectable LiI λ 6708 line, with the exception of TYC 4279-1821-1, which exhibits high photospheric abundances in both components. Photometric time series from the literature allowed us to assess that the five systems with a nearly circular orbit have also photometric periods close or equal to the orbital ones, indicating spin-orbit synchronization. For the system with a highly eccentric orbit, a possible pseudo-synchronization with the periastron velocity is suggested.

Key words: Binaries: spectroscopic – X-rays: stars – Stars: chromospheres – Stars: fundamental parameters – Stars: late-type – Stars: individual: TYC 3386-868-1, G 137-52, BD+10 2953, V1079 Her, BD+62 1880, TYC 4279-1821-1.

1 INTRODUCTION

X-ray emission is nowadays one of the best and accessible indicators of high-energy phenomena in stellar atmospheres and circumstellar environments. It is particularly useful to detect magnetic activity in late-type (FGKM) stars. Large area surveys, such as the ROSAT All-Sky Survey (RASS, Voges et al. 1999) and the 3XMM-DR7 catalogue (Traulsen et al. 2019), are ideal tools for the identification of young and/or active stars.

During the course of a survey of stellar X-ray sources selected by the cross-correlation of the RASS and TYCHO (Esa 1997) catalogues (henceforth the *RasTyc* sample), Guillout et al. (2009) and Frasca et al. (2018) discovered a number of double-lined spectroscopic binaries (SB2s) and multiple systems. Unlike single objects, which are mainly young main-sequence (MS) stars, the high X-ray activity level

for close binaries is often caused by the tidal synchronization of orbital and rotation motions that forces the components of these system to spin faster, enhancing the dynamo action. The most active binaries are those of the RS CVn type, which have periods from a few days to a few tens of days and contain at least one evolved (giant or subgiant) component (e.g., Hall 1976; Eker et al. 2008, and references therein). However, binaries composed of young MS stars, as witnessed by photospheric lithium in both components, which are likely BY Dra variables, are also present in X-ray selected samples.

Close binaries, especially spectrophotometric ones, are very important because they allow us to derive the basic physical properties of their components, such as effective temperatures, radii, and masses.

In this paper we present spectroscopic follow-up observations of six double-lined binaries, five of which were recently discovered by Frasca et al. (2018) during a spectroscopic survey of *RasTyc* faint sources.

[★] Based on observations made with the Catania Astrophysical Observatory Spectropolarimeter (CAOS) operated by the Catania Astrophysical Observatory.

[†] E-mail: antonio.frasca@inaf.it

Table 1. Parameters of the investigated binaries from the literature.

Name	RA (2000) h m s	DEC (2000) ° ' "	V^a (mag)	$B-V^a$ (mag)	π^b (mas)	μ_α^b (mas/yr)	μ_δ^b (mas/yr)	X-ray source IRXS	Counts (ct/s)
TYC 3386-868-1	06 04 51.40	+51 42 00.8	9.35	0.909	3.3728 ± 0.0176	15.033	-18.929	J060452.0+514200	1.51×10^{-1}
G 137-52	15 47 11.90	+15 09 14.9	9.61 ^c	0.99 ^c	17.9781 ± 0.0262	188.888	-365.224	J154712.0+150912	2.57×10^{-1}
BD+10 2953	16 05 02.23	+10 28 54.6	9.21	0.755	4.4293 ± 0.0203	-16.550	11.350	J160501.0+102843	6.00×10^{-2}
V1079 Her	16 20 13.72	+24 36 11.1	9.48	1.111	2.4434 ± 0.0134	-5.402	-3.449	J162013.2+243606	2.94×10^{-1}
BD+62 1880	20 58 16.40	+63 17 38.8	9.75	0.614	7.9306 ± 0.0130	67.637	84.592	J205814.0+631750	4.08×10^{-2}
TYC 4279-1821-1	23 22 40.03	+61 13 33.3	9.90	0.781	3.1552 ± 0.0113	-7.357	-16.165	J232241.3+611335	9.92×10^{-2}

^a V magnitude and $B-V$ color from the TYCHO catalogue (Esa 1997).

^b Parallax and proper motions from *Gaia*-EDR3 (Gaia Collaboration et al. 2021).

^c From Ryan (1989).

2 OBSERVATION AND DATA REDUCTION

Time-resolved spectroscopy was carried out at the *Catania Astrophysical Observatory Spectropolarimeter* (CAOS) which is a fiber fed, high-resolution, cross-dispersed échelle spectrograph (Catanzaro et al. 2015; Leone et al. 2016) installed at the Cassegrain focus of the 91 cm telescope of the “*M. G. Fracastoro*” observing station of the Catania Astrophysical Observatory (Mt. Etna, Italy). A number of spectra were obtained from 2015 to 2021 with exposure times ranging from 1200 to 2400 sec. For the best exposed spectra the signal-to-noise ratio (SNR) was at least 50 in the continuum in the 4300–7000 Å wavelength range. The spectral resolution of CAOS is $R \simeq 45\,000$, as we have verified from the full width at half maximum (FWHM) of the emission lines of the Th-Ar calibration lamp or the telluric absorption lines.

The reduction of spectra, which included the subtraction of the bias frame, trimming, correcting for the flat-field and the scattered light, extraction of the orders, and wavelength calibration, was done using the NOAO/IRAF packages¹.

We used also radial velocities previously collected by us with other two instruments, namely SARG at the 3.5 m TNG telescope (Observatorio del Roque de los Muchachos, Canary Islands, Spain) and AURELIE at the 1.52 m telescope at the Observatoire de Haute Provence (OHP, France). These data, which allowed us to classify these objects as SB2s, were published in Frasca et al. (2018).

Table 1 displays the observed targets along with photometric and astrometric data from the literature.

3 DATA ANALYSIS AND RESULTS

3.1 Radial velocity

The radial velocity (RV) was measured by cross-correlating targets and template spectra. The latter are ATLAS9 (Kurucz 1993) synthetic spectra with a solar metallicity and T_{eff} in the range 4000–6000 K that are calculated with SYNTHÉ (Kurucz & Avrett 1981) at the same resolution and sampling of the CAOS ones. For this purpose we used the IRAF task FXCOR (Tonry & Davis 1979; Fitzpatrick 1993). We excluded broad spectral features, such as Balmer and

NaI D₂ lines, because they blur the cross-correlation function (CCF) and hamper the measure of the RVs of the two components. The spectral ranges heavily affected by telluric absorption lines were discarded as well.

For each spectrum, the centroids of the CCF peaks of the two components are obtained by fitting two Gaussians, which allows us to disentangle the two peaks in cases of partial line blending. At orbital phases very close to the conjunctions, where the spectral lines of the two components are fully superposed, only one CCF peak is visible and the single Gaussian fitting provides a “blended” RV value, which is close to the barycentric velocity of the system.

The radial velocity measurements of these binaries are reported in Tables A1–A6 along with their errors (σ_{RV}). The latter were computed by FXCOR according to the fitted peak height and the antisymmetric noise as described by Tonry & Davis (1979). The observed RV curves are displayed in Fig. 1, where we used filled symbols for the primary (more luminous) components and open symbols for the secondary ones. With the exception of V1079 Her, which is composed of very similar stars with a mass ratio close to 1, the primary components are also the more massive ones. The RVs obtained in fully blended situations are marked with green crosses in Fig. 1. We used periodogram analysis (Scargle 1982) and the CLEAN deconvolution algorithm (Roberts et al. 1987), which allowed us to reject aliases generated by the spectral window of the unevenly sampled data, to determine the orbital periods from the RV variations of the SB2’s components. Then, we fitted the observed RV curve with the IDL² routine CURVEFIT (e.g., Bevington & Robinson 2003), adopting the function HELIO_RV for spectroscopic binaries with eccentric orbits, to determine the orbital parameters and their standard errors. The RV curve fitting also allowed us to improve the determination of the orbital period. The orbital solutions are overplotted to the RV data in Fig. 1.

The orbital period (P_{orb}), barycentric velocity (γ), eccentricity (e), longitude of periastron (ω), RV semi-amplitudes (k), masses ($M \sin^3 i$), and mass ratios (M_P/M_S) for each binary system are listed in Table 2, where P and S refer to the primary (more luminous) and secondary components of the SB2 systems, respectively.

¹ IRAF is distributed by the National Optical Astronomy Observatory, which is operated by the Association of Universities for Research in Astronomy, Inc.

² IDL (Interactive Data Language) is a registered trademark of Harris Corporation.

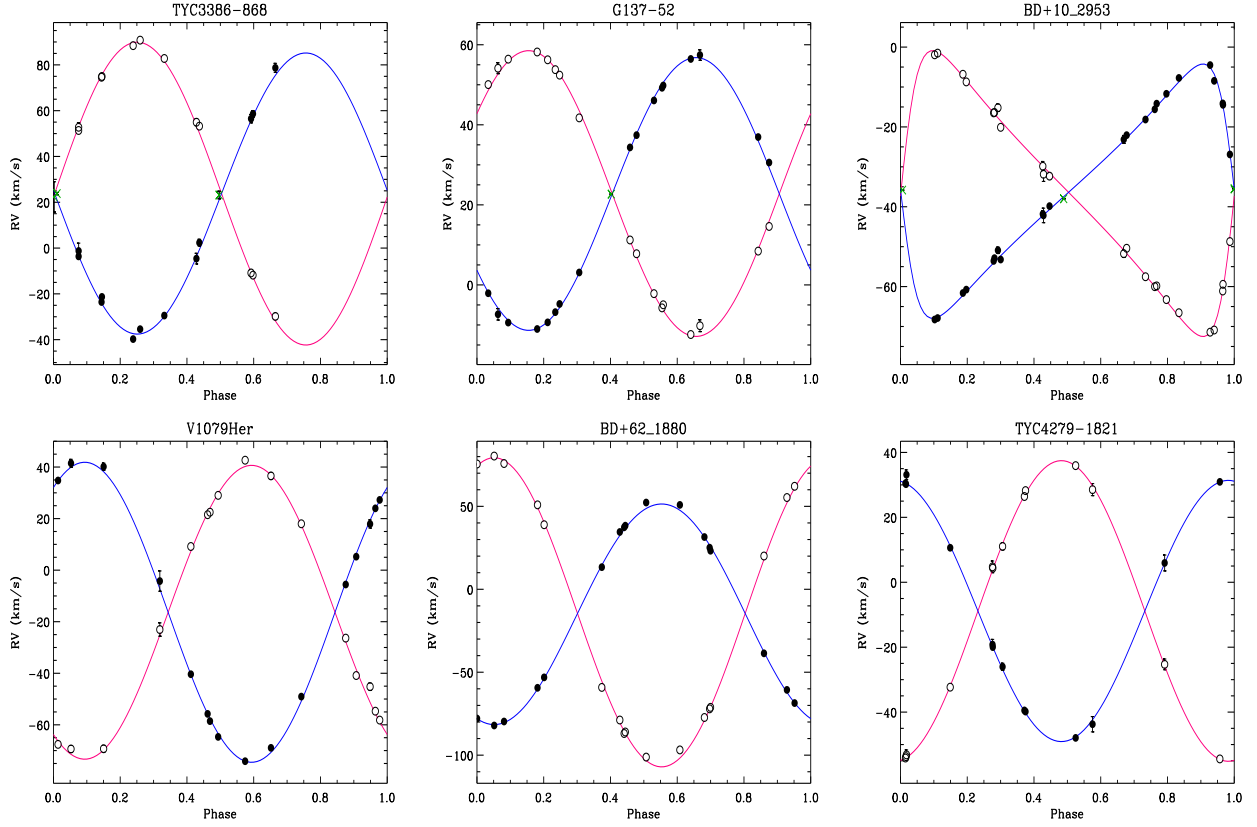


Figure 1. Radial velocity curves of the six *RasTyc* binaries. Filled and open symbols for the primary (more luminous) and secondary components have been used, respectively. The green crosses relate to the RV measured near the conjunctions, when only one peak is visible in the cross-correlation function. The blue and red lines represent the orbital solutions for the primary (more luminous) and secondary components, respectively.

Table 2. Orbital parameters of the *RasTyc* binaries.

Name	HJD0 ^a (2 450 000+)	P_{orb} (days)	e	ω ($^{\circ}$)	γ (km s^{-1})	k (km s^{-1}) [P/S]	$M \sin^3 i$ (M_{\odot}) [P/S]	$M_{\text{P}}/M_{\text{S}}$
TYC 3386-868-1	4453.68(5)	13.8204(1)	0.015(5)	88(5)	23.8(2)	61.4(3)/66.1(2)	1.54(1)/1.43(1)	1.077(5)
G 137-52	2436.02(4)	5.04823(1)	0.027(1)	124(3)	22.77(2)	34.07(4)/35.70(7)	0.0910(4)/0.0868(3)	1.048(2)
BD+10 2953	4105.33(3)	33.5251(3)	0.510(1)	269.0(2)	-36.38(2)	31.86(3)/35.82(5)	0.363(1)/0.323(1)	1.124(2)
V1079 Her	2421.0726(1)	19.4085(1)	0.000(1)	326.3(1)	-16.34(6)	58.2(1)/57.0(2)	1.524(9)/1.556(7)	0.980(3)
BD+62 1880	7258.92(2)	3.79074(1)	0.008(3)	161(1)	-14.57(5)	66.49(8)/93.20(24)	0.936(5)/0.667(3)	1.402(2)
TYC 4279-1821-1	2214.4952(6)	15.55528(1)	0.0000(2)	6.46(2)	-8.85(6)	40.24(8)/46.31(11)	0.560(3)/0.487(2)	1.151(3)

The errors on the last significant digit are enclosed in parenthesis. P=Primary (more luminous), S=Secondary.

^a Heliocentric Julian Date (HJD) of the periastron passage.

3.2 Atmospheric parameters

For the determination of the atmospheric parameters (T_{eff} and $\log g$) and to perform an MK classification of the components of these binary systems we used COMPO2 (Frasca et al. 2006, 2021). This code was developed in IDL environment and uses a grid of templates to reproduce the observed composite spectrum. As templates we adopted spectra of slowly rotating, low-activity stars retrieved from the ELODIE Archive (Moultaka et al. 2004), whose atmospheric parameters are known from the literature and listed in the PASTEL cata-

logue (Soubiran et al. 2010). The grid is composed of spectra of 90 stars both on the main sequence (FGKM types) and G-K giants.

For each binary system, we have chosen the spectrum with the best SNR and a large wavelength separation between the lines of the components, as derived from the CCF analysis. We have analyzed 39 échelle orders that cover the wavelength range 4290–6720 Å. The projected rotation velocities, $v \sin i_1$ and $v \sin i_2$, were measured by Frasca et al. (2018, table A.2) from the FWHM of the peaks of the CCF and are kept fixed

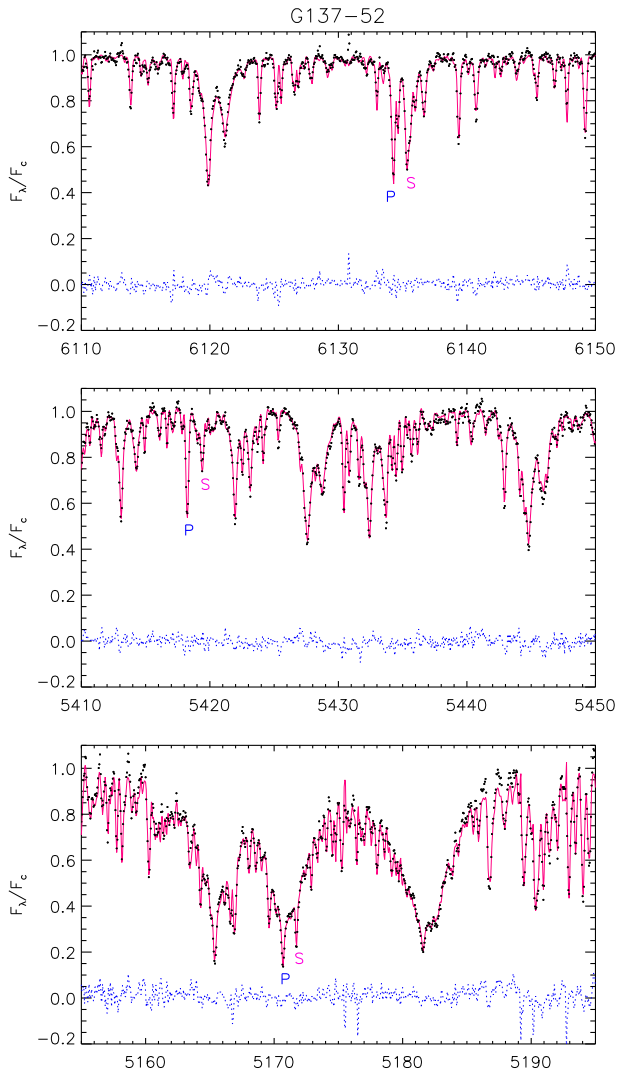


Figure 2. Example of spectral synthesis with COMPO2. In each panel the continuum-normalized spectrum of G 137-52 is plotted with black dots and it is overlaid to the synthetic spectrum (red lines) built up with the Doppler-shifted spectra of two standard stars mimicking the two components. The residuals are shown with blue dotted lines in the bottom of each panel. A few spectral lines of the primary and secondary component are also marked.

in the fit. The rotationally-broadened templates are shifted in wavelength according to the RV measured as described in Section 3.1 and summed, after weighting them according to their contribution to the local continuum. The flux ratio, i.e. the flux contribution of the primary component in units of the continuum, w^P , is an adjustable parameter. An example of the application of COMPO2 is shown in Fig. 2 for three spectral segments of a spectrum of G 137-52.

To evaluate the atmospheric parameters (APs), per each spectral segment we kept, among the 8100 possibilities, only the best 100 combinations (in terms of minimum χ^2) of primary and secondary spectra. To calculate the average APs, the results for individual segments have been weighted with the χ^2 of the fit and the total line absorption, $f_i = \int (F_\lambda/F_C - 1)d\lambda$, where F_λ/F_C is the continuum-normalized

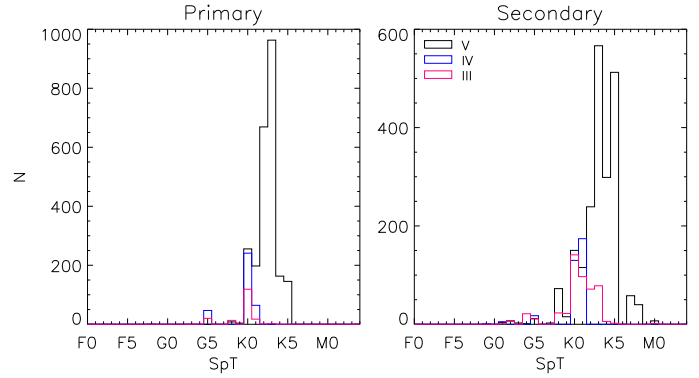


Figure 3. Distribution of spectral types for the components of G 137-52.

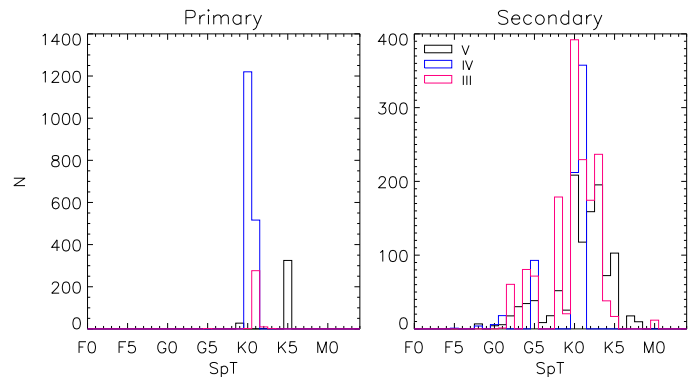


Figure 4. Distribution of spectral types for the components of V1079 Her.

spectrum in the i -th spectral segment. This parameter is an index of the amount of spectral information contained in each segment. Usually, the blue spectral regions have more and deeper lines than the red ones (higher f_i), but their SNR and the χ^2 of the fit are worse, which reduces their weight in the mean.

The APs are listed in Table 3. Averages values of w^P have been evaluated at three wavelengths (4600 Å, 5500 Å, and 6400 Å) by keeping only the spectral segments around these wavelengths. As can be seen in Table 3, w^P changes appreciably with wavelength for systems with components of very different T_{eff} , like TYC 3386-868-1, BD+10 2953, TYC 4279-1821-1, and BD+62 1880. For the latter, the flux of the primary component is much larger than the secondary one at all wavelengths. The spectral types (SpT) of the components are taken as the mode of the spectral-type distributions (Figs. 3 and 4 for two examples of binaries with MS and evolved components, respectively).

3.3 Hertzsprung-Russel diagram

In order to evaluate the consistency of the dynamical masses, previously determined, and the evolutionary ones, inferred from theoretical models, we constructed the Hertzsprung-Russel (HR) diagram.

We adopted the temperatures derived with COMPO2 and

Table 3. Physical parameters of the systems' components derived in the present work. $v \sin i$ values are from Frasca et al. (2018).

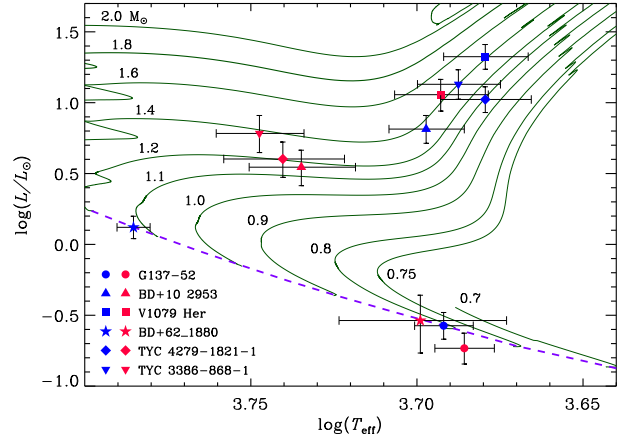
Name	$v \sin i$ (km s^{-1}) [P/S]	SpT [P/S]	w_{4600}^P	w_{5500}^P	w_{6400}^P	T_{eff} (K) [P/S]	$\log g$ (dex) [P/S]
TYC 3386-868-1	28.7/4.9	K1III/G5IV	0.55 ± 0.05	0.64 ± 0.05	0.77 ± 0.05	$4870 \pm 140 / 5590 \pm 170$	$2.93 \pm 0.33 / 4.05 \pm 0.26$
G 137-52	$< 5 / < 5$	K3V/K4V	0.65 ± 0.03	0.64 ± 0.02	0.62 ± 0.03	$4920 \pm 100 / 4850 \pm 100$	$4.57 \pm 0.14 / 4.50 \pm 0.28$
BD+10 2953	10.5/5.0	K0IV/G5IV	0.54 ± 0.03	0.60 ± 0.05	0.65 ± 0.15	$4980 \pm 130 / 5430 \pm 200$	$3.34 \pm 0.66 / 3.87 \pm 0.38$
V1079 Her	18.2/19.6	K0IV/K1III-IV	0.64 ± 0.03	0.63 ± 0.02	0.59 ± 0.04	$4780 \pm 140 / 4930 \pm 160$	$3.04 \pm 0.29 / 3.50 \pm 0.82$
BD+62 1880	11.4/19.0	F9V/K0V	0.90 ± 0.07	0.85 ± 0.05	0.80 ± 0.07	$6100 \pm 70 / 5000 \pm 290$	$4.16 \pm 0.11 / 4.22 \pm 0.47$
TYC 4279-1821-1	10.6/8.2	K0IV/G5IV	0.43 ± 0.05	0.57 ± 0.05	0.67 ± 0.06	$4780 \pm 150 / 5500 \pm 230$	$3.21 \pm 0.52 / 4.14 \pm 0.29$

listed in Table 3. The luminosities of the components of the SB2 systems, $L_{P,S}$, were derived from the combined V magnitude listed in Table 1 and the luminosity ratio at 5500 Å (which is related to w_{5500}^P in Table 3). The values of V have been corrected for the extinction, A_V , and have been used to calculate the absolute magnitudes in the V band, M_V , with the *Gaia* distances (d). The latter have been estimated by direct inversion of the parallax, after having been corrected according to the recommendations outlined by Lindegren et al. (2021). Once distances and positions in the sky were known, the A_V for each system was determined from the maps of extinction obtained by Lallement et al. (2019). For these bright and relatively nearby sources, the values of extinction are rather low ($A_V = 0.01 - 0.31$ mag, Table 4).

The bolometric correction of Pecaut & Mamajek (2013) was applied to get the bolometric magnitudes from the values of M_V . Finally, the bolometric magnitude of the Sun, $M_{\text{bol}}^{\odot} = 4.64$ mag (Cox 2000), was used to express the stellar luminosity in solar units. The error of luminosity includes the parallax error, the error on w_{5500}^P , and the uncertainty on the V_0 magnitude. The latter includes the error on the extinction, which has been estimated as 0.2 mag.

The HR diagram for the components of the six *RasTyc* binaries, represented with different symbols, is shown in Fig. 5 where the PARSEC evolutionary tracks (Bressan et al. 2012) for a solar metallicity ($Z=0.017$) are displayed with continuous lines. This diagram confirms the MS stage for both components of G 137-52 and BD+62 1880, in agreement with their MK spectral classification. The secondary components of TYC 3386-868-1, BD+10 2953, and TYC 4279-1821-1, which we classified all as G5IV, are correctly located in the region of the HR occupied by subgiant stars, while the remaining stars lie in the red-giant branch. Their masses are in the range 1–2 M_{\odot} .

Comparing the masses of the two components of each system, which can be inferred for their position on the HR diagram (quoted in Table 4), with the dynamical masses $M_{P,S} \sin^3 i$ (Table 2), we can derive the inclination, i , of these systems. The values of i derived from the two components of each system agree very well, within 3–5°, with each other. The average value is reported in Table 4. There are only two cases where the masses of the components derived from the HR diagram are smaller than (but nearly equal to) the dynamical masses $M_{P,S} \sin^3 i$, implying $\sin i > 1$, namely TYC 3386-868-1 and V1079 Her. In these cases we have quoted an inclination of 90° in Table 4. However, the mass uncertainty of 0.15–0.30 M_{\odot} for these stars (Table 4) allows for lower values of inclination down to $i \sim 75^\circ$, for


Figure 5. HR diagram. Blue and red symbols are used for the primary and secondary components, respectively. Evolutionary tracks with solar metallicity ($Z=0.017$) from Bressan et al. (2012) are overlaid by continuous lines. The Zero Age Main Sequence (ZAMS) at $\tau=200$ Myr is shown by a purple dashed line.

which these systems with large separations should not display eclipses, in agreement with the behaviour of their light curves (see Section 5). Moreover, if we consider larger values of extinction, like those of $A_V=0.47$ mag and 0.26 mag reported by Gontcharov & Mosenkov (2018) for TYC 3386-868-1 and V1079 Her, respectively, the inconsistency between dynamical and evolutionary masses disappears.

4 CHROMOSPHERIC EMISSION AND LITHIUM CONTENT

The level of chromospheric activity can be evaluated from the emission in the core of the $H\alpha$ line. The detection of chromospheric emission in the $H\alpha$ line core is not a trivial task for SB2 systems which display spectral lines of both components, with a different rotational broadening that are Doppler shifted at different wavelengths according to the orbital phase. To this end, we subtracted the composite spectra produced by COMPO2 with non-active templates from the observed spectra of the targets, to remove the underlying photospheric lines so as to leave as residual chromospheric emission that fills the $H\alpha$ cores of one or both components. The same composite templates were also subtracted to the observed spectra to measure the equivalent width of the $\text{Li I } \lambda 6708 \text{ \AA}$ absorption line (EW_{Li}), removing

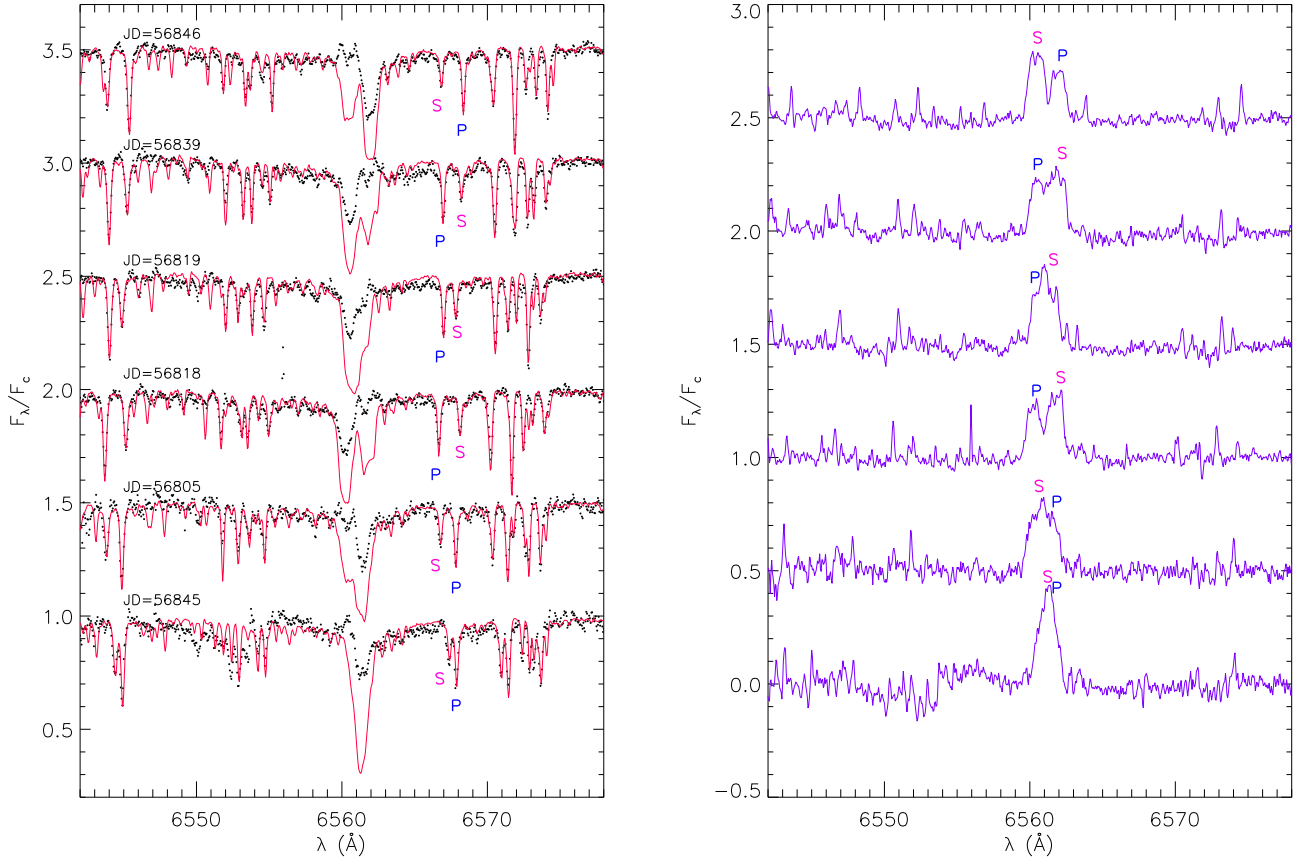


Figure 6. Sample of CAOS spectra of G 137-52 in the $H\alpha$ region taken at different orbital phases. *Left panel*) Synthetic composite spectra (red lines) are overlaid with the observed spectra (black dots) taken at the Julian date marked on top on each spectrum. The position of the $\text{Fe I } \lambda 6569 \text{ \AA}$ line of the primary (P) and secondary (S) component is also marked in each spectrum. The chromospheric emission which fills in the $H\alpha$ core of both components is clearly visible in the subtracted spectra (*right panel*) where the $H\alpha$ wavelength of the primary and secondary component is also marked.

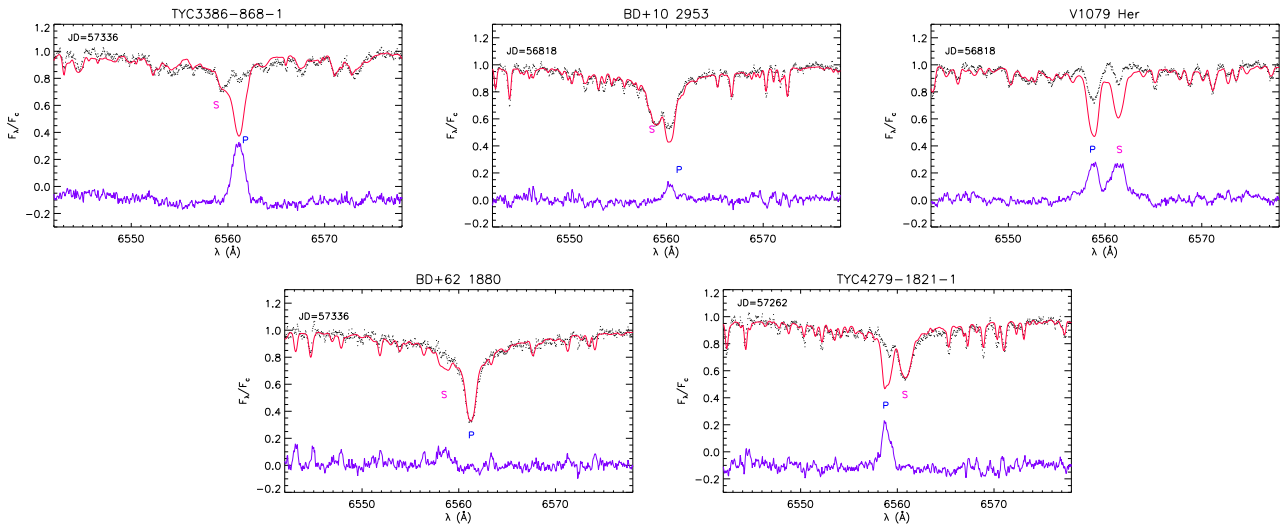


Figure 7. CAOS spectra of the investigated systems in the $H\alpha$ region. In each box, the synthetic composite spectra (red lines) are overlaid with the observed spectra (black dots). The position of the $H\alpha$ line of the primary (P) and secondary (S) components are also marked. The chromospheric emission which fills in the $H\alpha$ core of one or both components is clearly visible in the subtracted spectra (purple line in the bottom of each panel).

Table 4. Physical parameters related to or inferred from the HR diagram.

Name	d (pc)	A_V (mag)	L_P (L_\odot)	L_S (L_\odot)	M_P (M_\odot)	M_S (M_\odot)	i^a ($^\circ$)
TYC 3386-868-1	293.6	0.257	13.482±3.252	6.069±1.837	1.40 ^{+0.20} _{-0.30}	1.38 ^{+0.10} _{-0.15}	90
G 137-52	55.5	0.006	0.267±0.058	0.185±0.047	0.82 ^{+0.05} _{-0.10}	0.77 ^{+0.05} _{-0.10}	30
BD+10 2953	224.2	0.044	6.511±1.476	3.508±1.012	1.35 ^{+0.15} _{-0.25}	1.18 ^{+0.12} _{-0.13}	40
V1079 Her	404.7	0.169	21.114±4.257	11.391±2.937	1.42 ^{+0.30} _{-0.30}	1.45 ^{+0.20} _{-0.25}	90
BD+62 1880	125.8	0.014	1.320±0.241	0.290±0.133	1.12 ^{+0.05} _{-0.05}	0.83 ^{+0.08} _{-0.15}	70
TYC 4279-1821-1	314.8	0.313	10.535±2.212	4.007±1.152	1.10 ^{+0.30} _{-0.25}	1.20 ^{+0.15} _{-0.10}	50

^a Derived from the comparison between the evolutionary masses, $M_{P,S}$, inferred from the position on the HR diagram and the dynamical masses listed in Table 2.

the blends with nearby lines. With the exception of TYC 4279-1821-1, which displays LiI absorption from both components, for the remaining systems no lithium line could be clearly detected (see Fig. 8). Based on the noise in the residual spectrum, we estimate upper limits of about 30 mÅ for EW_{Li} in the latter cases. In the best residual spectra of TYC 4279-1821-1 we have measured $EW_{Li} = 95 \pm 30$ mÅ and 92 ± 30 mÅ for the primary and secondary component, respectively. These values must be divided by the contribution to the red continuum of the respective component, $w_{6400}^P = 0.67$ and $w_{6400}^S = 0.33$, getting the correct values $EW_{Li}^P = 140$ mÅ and $EW_{Li}^S = 280$ mÅ. We calculated the lithium abundance, $A(Li)$, from our values of T_{eff} , $\log g$, and EW_{Li} by interpolating the curves of growth of Lind et al. (2009), which span the T_{eff} range 4000–8000 K and \log from 1.0 to 5.0 and include non-local thermal equilibrium corrections. For the stars without LiI detection, we have always found an abundance $A(Li) < 2$, while we found $A(Li) = 2.2$ and 3.1 for the primary and secondary component of TYC 4279-1821-1, respectively. These abundances are larger than the typical values measured in single giants, but are in the range of those displayed by the so-called lithium-rich giants ($A(Li) \geq 1.4$, e.g., Smiljanic et al. 2018; Martell et al. 2021, and reference therein) and by some active binaries (e.g., Pallavicini et al. 1992; Randich et al. 1993). In particular, Randich et al. (1993, 1994) found that the evolved components of spectroscopic binaries present an excess Li abundance with respect to single stars of the same spectral type. However, they found high values of $A(Li)$ only for a fraction of systems and moderate abundances ($A(Li) \leq 1.5$) for most systems, with no obvious dependence on activity parameters such as rotation and chromospheric emission. Therefore, they suggest that activity *per se* is likely not the cause of the enhanced Li abundance. This is also displayed by the four binaries of the present paper, whose evolved components have a comparably high level of chromospheric activity, but a high Li abundance has been measured only for TYC 4279-1821-1. Anyway, the issue of atmospheric lithium overabundance in binaries is very complex also due to different effects related to evolution, activity, and binarity, which are simultaneously at work. For instance, Barrado y Navascues et al. (1998) show that a significant part of the evolved components of the binaries studied by them have lithium excesses, independently of their mass and evolutionary stage. They find instead the Li overabundance to be closely related to the stellar rotation, and interpret it as a consequence of the transfer of angular momentum from the orbit to the rotation as the stars evolve

in and off the Main Sequence. They suggest that the angular momentum transfer reduces the differential rotation and the related turbulent internal mixing with a consequent reduction of the rate of Li depletion. This is supported by the measure of lithium abundance in binaries belonging to the Hyades and M67 open clusters, which display higher $A(Li)$ compared to the single stars of the same cluster. A relation of $A(Li)$ with the stellar rotation for the components of active binaries, although with a large scatter, has been also found by Strassmeier et al. (2012).

Deriving accurate ages of pre-main sequence (PMS) and MS stars from the atmospheric lithium content is not a straightforward task (e.g., Leone 2007; Franciosini et al. 2022). This task is even more complicated in the case of binary systems (e.g., Giarrusso et al. 2016; Frasca et al. 2019). A broad age classification for single stars and the components of SB2s can be instead carried out with the help of the upper envelopes of the lithium abundance distributions for members of open clusters (e.g., Gutiérrez Albarrán et al. 2020, and references therein). We note that the upper limits of both EW_{Li} and $A(Li)$ indicate that the MS components of the systems studied in the present work are older than about 1 Gyr (e.g., Randich 2009; Jeffries 2014; Gutiérrez Albarrán et al. 2020), suggesting that the high level of chromospheric and coronal activity observed in these objects is not an age effect, but it is rather the result of the spin-orbit synchronization.

The spectral subtraction in the H α region reveals that both components of G 137-52 are chromospherically active, with the less-massive cooler one displaying the stronger emission, which is just above the local continuum in most spectra (Fig. 6). The same behaviour is displayed by V1079 Her which hosts two very active K-type giants (Fig. 7). For TYC 3386-868-1, BD+10 2953, and TYC 4279-1821-1, which have the typical composition (K0-1 IV-III/G5IV) of RS CVn systems, the emission is clearly detected only for the cooler (brighter and more massive) components (Fig. 7). The same holds true for BD+62 1880, a system composed of main-sequence stars, where H α emission is only seen at the wavelength of the cooler K0V component, while the F9V primary does not show any filling in its H α core.

5 NOTES ON INDIVIDUAL OBJECTS

5.1 TYC 3386-868-1

This object is classified as a variable source in the All Sky Automated Survey for SuperNovae (ASAS-SN) catalogue

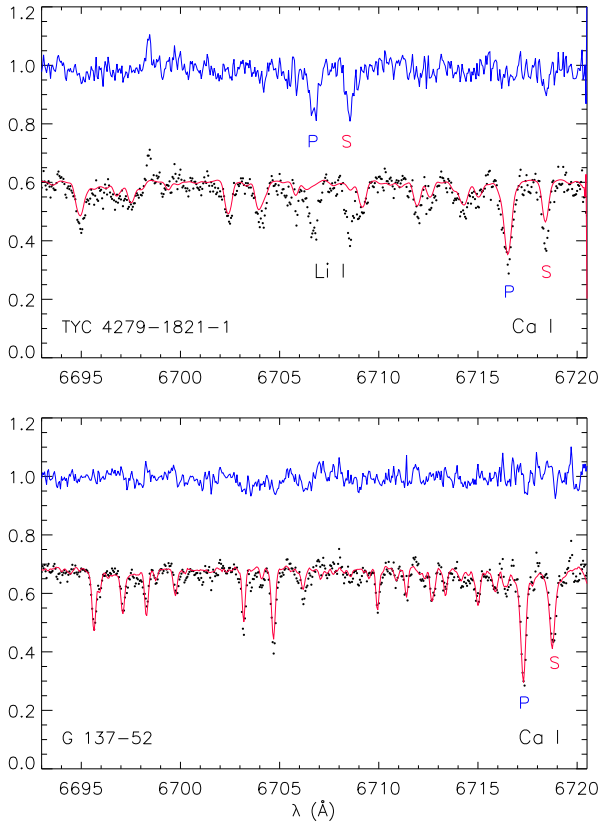


Figure 8. *Upper panel*) Subtraction of the synthetic composite spectrum (red line) from one observed spectrum of TYC 4279-1821-1 (black dots), which emphasizes the Li I $\lambda 6708 \text{ \AA}$ absorption lines of the two components, marked near the residual spectrum (blue line) with ‘P’ and ‘S’ for the primary and secondary component, respectively. *Lower panel*) Observed (black dots) and synthetic composite spectrum (red line) of G 137-52. The position of the Ca I $\lambda 6717 \text{ \AA}$ lines of the primary and secondary component is marked. The Li I lines of the two components are not detectable either in the observed or in the residual spectrum.

(Jayasinghe et al. 2019), which reports an amplitude of 0.45 mag and a period of 399 days. The latter is not the rotational period, but it is rather related to long-term variations of the starspot distribution. The catalog of All Sky Automated Survey (ASAS) photometry of ROSAT sources-II (Kiraga & Stepień 2013) lists a variation amplitude of 0.15 mag and a more reliable period of 13.63 days, which is close to the orbital one measured by us. The orbital solution indicates a very low eccentricity that, according to Lucy & Sweeney (1971), can be considered as zero.

The timescales for circularization and synchronization, calculated for the primary component according to Zahn (1989), are $\tau_{\text{circ}} \sim 3 \text{ Myr}$ and $\tau_{\text{sync}} \sim 0.05 \text{ Myr}$, respectively. This is in line with the observations that indicate a synchronous system with a nearly circular orbit. The spectral subtraction reveals $H\alpha$ emission only from (or predominantly from) the cooler, more massive component. This is not surprising, considering the larger stellar radius that we estimate for this star ($\sim 5R_{\odot}$) compared to the secondary component ($\sim 2.5R_{\odot}$), which implies a larger equatorial velocity for the primary component, as also indicated by the values of the projected rotational

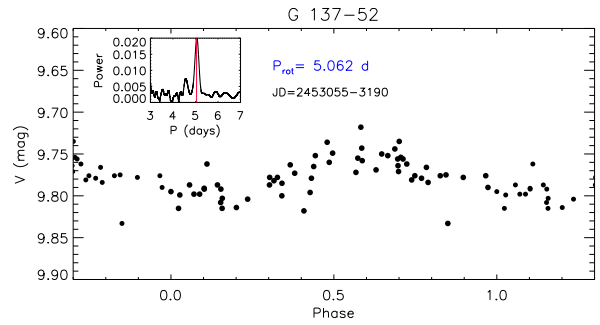


Figure 9. Phased V-band ASAS light curve of G 137-52 from 19 February to 3 July 2004. The inset shows the cleaned periodogram of these data; the orbital period is marked with a vertical red line.

velocity (see Table 3). This is producing a stronger dynamo action on sub-photospheric layers of the primary component, which is responsible for the higher level of magnetic activity, similarly to what is observed in well-known RS CVn systems like HR 1099, WW Dra, and UX Ari (e.g., Frasca & Catalano 1994; Montes et al. 1995), whose components have similar SpT as TYC 3386-868-1.

5.2 G 137-52

In addition to X-ray emission, this star is also an extreme ultraviolet source included in the 2RE Source Catalogue (Pye et al. 1995) with the name 2RE J1547+150. It was already discovered as an SB2 by Jeffries et al. (1995) who obtained intermediate-dispersion spectra in a spectral range around the $H\alpha$ line. They also present a poorly sampled radial velocity curve (also due to the orbital period almost equal to 5 days) with relatively large errors ($2\text{--}4 \text{ km s}^{-1}$) and a solution with orbital parameters close to those found by us. In their spectra, the $H\alpha$ line displays a filled-in profile, but, without a subtraction of a photospheric template, they cannot say anything about the chromospheric activity level of both components. From our spectra the secondary component displays a stronger filling of the $H\alpha$ line which, in some spectra, is just above the local continuum.

No information on photometric period can be found in the literature, by seeking in the VizieR database. We thus searched for periods in the ASAS photometry available for this source with the cleaned periodogram analysis. We found periods ranging from 4.99 to 5.13 days by analyzing different data segments with length shorter than 300 days (see Fig. 9). A peak at $P_{\text{rot}} = 5.01 \text{ days}$ is clearly visible in the whole time series. Therefore, G 137-52 appears to be a synchronous system in a nearly circular orbit. This is in line with the timescales for circularization and synchronization, which are $\tau_{\text{circ}} \sim 5 - 10 \text{ Gyr}$ and $\tau_{\text{sync}} \sim 15 \text{ Myr}$, respectively.

5.3 BD+10 2953

This object is classified as a variable source in the ASAS photometry of ROSAT sources-I catalogue (Kiraga 2012), which reports a period of 12.19 days. The ASAS-SN catalogue (Jayasinghe et al. 2019) reports instead an amplitude of 0.15 mag and a period of 427 days, which is likely the result of long-term variations. Indeed, if we do a period search in

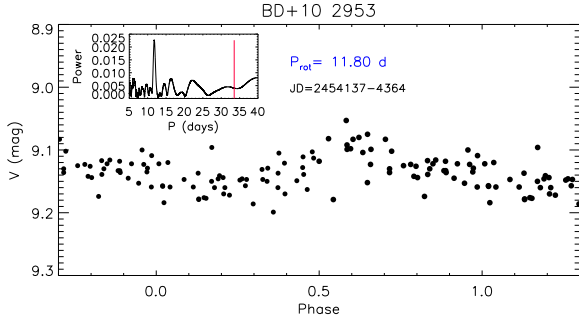


Figure 10. V-band ASAS light curve of BD+10 2953 from 5 February to 21 September 2007 phased with the photometric period of 11.80 days. The inset shows the cleaned periodogram of these data; the orbital period is marked with a vertical red line.

portions of ASAS-SN V data spanning less than one year, we find cleaned periodograms without strong and clear peaks. Some indication of a period of about 27.9 days emerges for the data in the Julian day range $JD=[2457020,2457250]$ and 30.3 days for $JD=[2457397,2457630]$, respectively. However, in both cases a rather low peak amplitude of ~ 0.025 mag was found. These periodicities are not far from the orbital period and might be related to the rotational modulation produced by starspots in one or both components or to proximity effects. A similar analysis applied to segments of the ASAS photometry provided results in agreement with those of (Kiraga 2012), since we found peaks of the cleaned periodograms in the range 11.6–12.4 days in different segments (see Fig. 10) and $P = 11.8$ days, as the second highest peak, in the full dataset.

The timescales for circularization and synchronization, calculated for the primary component according to Zahn (1989), are $\tau_{\text{circ}} \sim 2.3$ Gyr and $\tau_{\text{sync}} \sim 10$ Myr, respectively. For the secondary component a longer synchronization time, $\tau_{\text{sync}} \sim 100$ Myr, is found. As we did not detect the Lii $\lambda 6708$ absorption line from either component, the system should be much older than 10 Myr and even older than 100 Myr, which is close to the age of the Pleiades; therefore the system should have already attained the spin-orbit synchronization while the orbit is still highly eccentric. However, in an eccentric orbit the tidal interaction is stronger at periastron, when the orbital velocity is higher, with the consequence that the equilibrium is reached at a value of rotation period, P_{pseudo} , which is smaller than P_{orb} , leading to a pseudo-synchronization (see, e.g., Hut 1981). The value of P_{pseudo} depends on the orbital period and the eccentricity of the system and, following the guidelines of Hut (1981), results to be about 11.5 days for the components of BD+10 2953. The timescale for the pseudo-synchronization can be evaluated as $\tau_{\text{pseudo}} \sim 23$ Myr, which, according to the above arguments, is smaller than the system age. The pseudo-synchronization period, $P_{\text{pseudo}} \simeq 11.5$ days, is close to the period derived by Kiraga (2012) and by our analysis of the ASAS photometry ($P=11.6$ –12.4 days), but it has not been found in the ASAS-SN data. More precise photometry, like that one collected by space missions, will be crucial to confirm or reject the pseudo-synchronization status of this system.

The spectral subtraction reveals a moderate filling of the $H\alpha$ core of the primary component only.

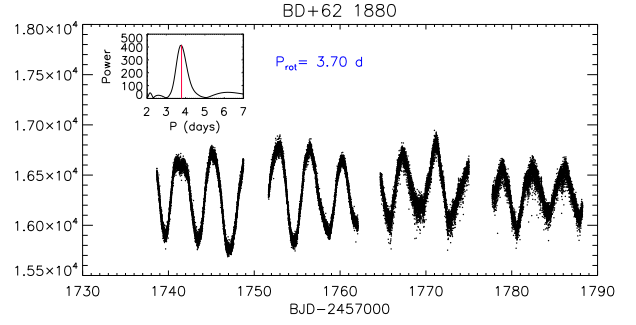


Figure 11. TESS light curve of BD+62 1880 in 2019. The inset shows the cleaned periodogram of these data; the orbital period is marked with a vertical red line.

5.4 V1079 Her

This star is included in the Hamburg/RASS Catalogue of optical identifications (Zickgraf et al. 2003), but the saturated prism-objective spectrum did not allow them to classify this object. Various period determinations can be found in the literature for this source, since from its discovery as a variable star by Robb et al. (2003), who report, from VRI photometry, a period of 19.1 days and suggest a spotted late-type giant. The ASAS catalogue of variable stars (Pojmanski 2002) reports a period of 18.97 days and an amplitude of 0.12 mag. Norton et al. (2007) quote a period of 18.5948 days from SuperWASP (Wide Angle Search for Planets) photometry. We have reanalysed the ASAS data finding a peak at 19.04 days. All these determinations are very close to the orbital period indicating that the spin-orbit synchronization has been attained in this system. Indeed, the timescales for circularization and synchronization are $\tau_{\text{circ}} \sim 20$ Myr and $\tau_{\text{sync}} \sim 0.2$ Myr, respectively.

The two components display also a comparable level of chromospheric activity as suggested by the similar intensity of the $H\alpha$ emission filling the cores of the profiles of the two components (Fig. 7).

5.5 BD+62 1880

No information on photometric period can be found in the literature, by seeking in the VizieR database of catalogs. Fortunately, space-born accurate photometry was obtained with NASA2019s Transiting Exoplanet Survey Satellite (TESS Ricker et al. 2015). This object was observed in sector 16 between 2019-09-12 and 2019-10-06, in sector 17 between 2019-10-08 and 2019-11-02, and in sector 24 between 2020-04-16 and 2020-05-12. The first two nearly consecutive datasets are plotted in Fig. 11 as a function of the barycentric Julian date (BJD) and display a clear rotational modulation. The cleaned periodogram, shown in the inset plot, displays a peak at 3.70 days, which is close to the orbital period of the system. The short timescale for synchronization, $\tau_{\text{sync}} \sim 4$ Myr, supports the results of the analysis of the TESS light curve.

The spectral subtraction (Fig. 7) shows $H\alpha$ emission from the secondary K0V component, while the primary F9V component does not display any significant filling in the core of the line.

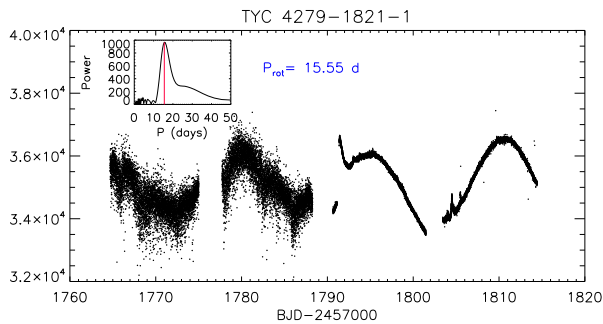


Figure 12. TESS light curve of TYC 4279-1821-1 in 2019. The inset shows the cleaned periodogram of these data; the orbital period is marked with a vertical red line.

5.6 TYC 4279-1821-1

The first optical identification of this X-ray source was made by [Motch et al. \(1998\)](#), who report a G0V SpT. It is located in the field of the open cluster NGC 7654, but neither its parallax nor its proper motions (see [Table 1](#)) are consistent with the average values for NGC 7654, which are $\pi = 0.596 \pm 0.002$ mas, $\mu_\alpha = -1.938 \pm 0.005$ mas/yr, and $\mu_\delta = -1.131 \pm 0.005$ mas/yr ([Cantat-Gaudin et al. 2018](#)). It was classified as an eclipsing binary with a period $P = 30.976$ days by [Laur et al. \(2017\)](#), but their light curve looks more like a rotational modulation with an amplitude of about 0.10 mag. It is worth noticing that this period is about twice the orbital one found by us and listed in [Table 2](#). A rotational period of 15.618 days is instead reported by [Watson et al. \(2006\)](#).

TYC 4279-1821-1 was observed by TESS in sector 17 between 2019-10-08, in sector 18 between 2019-11-03 and 2019-11-27, and in sector 24 between 2020-04-16 and 2020-05-12. The first two nearly consecutive datasets are plotted in [Fig. 12](#) as a function of the BJD and display a clear rotational modulation with a period of 15.55 days, which is exactly the orbital period, as also apparent from the peak of the periodogram. A few flares are visible in the more precise TESS light curve taken in sector 18. Therefore, this system appears to be synchronous and with a circular orbit, in line with the circularization and synchronization times, $\tau_{\text{circ}} \sim 5$ Myr and $\tau_{\text{sync}} \sim 0.1$ Myr.

As for TYC 3386-868-1 and other RSCVn systems, the H α emission is related to the cooler primary K0IV component, while the G5IV secondary does not display any significant filling of the line core.

As mentioned in [Section 4](#), this is the only system for which we could detect LiI λ 6708 absorption from both components. The equivalent width of the lithium line, corrected for the contribution to the continuum, is $EW_{\text{Li}}^{\text{P}} = 140$ mÅ and $EW_{\text{Li}}^{\text{S}} = 280$ mÅ, for the primary and secondary component, respectively, which give rise to lithium abundances of 2.2 and 3.1 dex.

6 CONCLUSIONS

In this work we have studied six spectroscopic binaries with X-ray emission, out of which five were recently discovered. We performed a high-resolution spectroscopic monitoring of our targets (TYC 3386-868-1, G 137-52, BD+10 2953, V1079 Her,

BD+62 1880, and, TYC 4279-1821-1), from 2015 to 2021, mainly with the CAOS spectropolarimeter. As a result, we obtained the radial velocity curve for each binary, and from its analysis we determined the orbital parameters of the pair. Additionally, we estimated the spectral type and atmospheric parameters for both components of the system. From the comparison of the dynamical masses (inferred from the orbital solution) and the evolutionary ones (estimated from the location of the stars in the HR diagram) we derived the inclination of the system.

We find that our targets correspond to low-mass stars with masses between 0.8 and 1.5 M_\odot and spectral types from F9 to K4. G 137-52 and BD+62 188 are composed of main sequence stars while in the remaining four systems are involved evolved stars, similar to that observed in binaries of the RSCVn type. For all observed stars, luminosity classes agree with the evolutionary stages, as evidenced by their positions in the HR diagram. The orbital periods of the MS binaries are the shortest (3.7–5.0 d), whereas for the four binaries with evolved components they are larger (13–33 d). All systems studied in this work follow nearly circular orbits with the exception of BD+10 2953, the system with the longest period, which exhibits a high eccentricity.

We also resorted to archival photometric data to search for photometric periods by means of periodogram analysis. For a few objects there were also period determinations in the literature. We found that the five systems with a nearly circular orbit have also photometric periods close or equal to the orbital ones, which indicates that these system have already attained spin-orbit synchronization. This is in line with the timescales for synchronization, which have been evaluated according to the prescription of [Zahn \(1989\)](#) and result to be always shorter than about 15 Myr, i.e. much less than the age of these systems, as inferred, e.g., from the atmospheric lithium content. The longest circularization times are found for G 137-52 ($\tau_{\text{circ}} \gtrsim 5$ Myr) and BD+10 2953 ($\tau_{\text{circ}} \gtrsim 2.3$ Myr). These systems are also those with the highest eccentricities. For BD+10 2953, which displays the most eccentric orbit ($e = 0.510$), a possible pseudo-synchronization with the periastron velocity is suggested.

Finally, we have also investigated the chromospheric activity finding that for G 137-52 and V 1079 Her both components are active. In the remaining four systems the H α emission is only visible in the cooler component. Additionally, none of the pairs show an appreciable amount of photospheric Li, with the exception of TYC 4279-1821-1, which exhibits high abundances in both components.

ACKNOWLEDGMENTS

This research has made use of the SIMBAD database and VizieR catalogue access tool, operated at CDS, Strasbourg, France.

This work has made use of data from the European Space Agency (ESA) mission *Gaia* (<https://www.cosmos.esa.int/gaia>), processed by the *Gaia* Data Processing and Analysis Consortium (DPAC, <https://www.cosmos.esa.int/web/gaia/dpac/consortium>). Funding for the DPAC has been provided by national institutions, in particular the institutions participating in the *Gaia* Multilateral Agreement.

This paper includes data collected by the TESS mission which are publicly available from the Mikulski Archive for Space Telescopes (MAST). Funding for the TESS mission is provided by the NASA 2019s Science Mission -Directorate. Support from the Italian *Ministero dell'Istruzione, Università e Ricerca* (MIUR) is also acknowledged.

DATA AVAILABILITY

The spectroscopic data underlying this paper will be shared on reasonable request to the corresponding author. TESS photometric data are available at <https://archive.stsci.edu/>.

REFERENCES

- Barrado y Navascues D., de Castro E., Fernandez-Figueroa M. J., Cornide M., Garcia Lopez R. J., 1998, *A&A*, **337**, 739
- Bevington P. R., Robinson D. K., 2003, Data reduction and error analysis for the physical sciences
- Bressan A., Marigo P., Girardi L., Salasnich B., Dal Cero C., Rubele S., Nanni A., 2012, *MNRAS*, **427**, 127
- Cantat-Gaudin T., et al., 2018, *A&A*, **618**, A93
- Catanzaro G., et al., 2015, *MNRAS*, **451**, 184
- Cox A. N., 2000, Allen's astrophysical quantities
- Eker Z., et al., 2008, *MNRAS*, **389**, 1722
- Esa ., 1997, VizieR Online Data Catalog, p. I/239
- Fitzpatrick M. J., 1993, in Hanisch R. J., Brissenden R. J. V., Barnes J., eds, *Astronomical Society of the Pacific Conference Series* Vol. 52, *Astronomical Data Analysis Software and Systems II*. p. 472
- Franciosini E., et al., 2022, *A&A*, **659**, A85
- Frasca A., Catalano S., 1994, *A&A*, **284**, 883
- Frasca A., Guillout P., Marilli E., Freire Ferrero R., Biazzo K., Klutsch A., 2006, *A&A*, **454**, 301
- Frasca A., Guillout P., Klutsch A., Ferrero R. F., Marilli E., Biazzo K., Gandolfi D., Montes D., 2018, *A&A*, **612**, A96
- Frasca A., et al., 2019, *A&A*, **632**, A16
- Frasca A., et al., 2021, *A&A*, **656**, A138
- Gaia Collaboration et al., 2021, *A&A*, **649**, A1
- Giarrusso M., et al., 2016, in *Journal of Physics Conference Series*. p. 012018, doi:10.1088/1742-6596/703/1/012018
- Gontcharov G. A., Mosenkov A. V., 2018, *MNRAS*, **475**, 1121
- Guillout P., et al., 2009, *A&A*, **504**, 829
- Gutiérrez Albarrán M. L., et al., 2020, *A&A*, **643**, A71
- Hall D. S., 1976, in Fitch W. S., ed., *Astrophysics and Space Science Library* Vol. 60, *IAU Colloq. 29: Multiple Periodic Variable Stars*. p. 287, doi:10.1007/978-94-010-1175-4_15
- Hut P., 1981, *A&A*, **99**, 126
- Jayasinghe T., et al., 2019, *MNRAS*, **485**, 961
- Jeffries R. D., 2014, in *EAS Publications Series*. pp 289–325 (arXiv:1404.7156), doi:10.1051/eas/1465008
- Jeffries R. D., Bertram D., Spurgeon B. R., 1995, *MNRAS*, **276**, 397
- Kiraga M., 2012, *Acta Astron.*, **62**, 67
- Kiraga M., Stepień K., 2013, *Acta Astron.*, **63**, 53
- Kurucz R. L., 1993, in Dworetzky M. M., Castelli F., Faraggiana R., eds, *Astronomical Society of the Pacific Conference Series* Vol. 44, *IAU Colloq. 138: Peculiar versus Normal Phenomena in A-type and Related Stars*. p. 87
- Kurucz R. L., Avrett E. H., 1981, *SAO Special Report*, 391
- Lallement R., Babusiaux C., Vergely J. L., Katz D., Arenou F., Valette B., Hottier C., Capitanio L., 2019, *A&A*, **625**, A135
- Laur J., Kolka I., Eenmäe T., Tuvikene T., Leedjärv L., 2017, *A&A*, **598**, A108
- Leone F., 2007, *ApJ*, **667**, L175
- Leone F., et al., 2016, *AJ*, **151**, 116
- Lind K., Asplund M., Barklem P. S., 2009, *A&A*, **503**, 541
- Lindegren L., et al., 2021, *A&A*, **649**, A4
- Lucy L. B., Sweeney M. A., 1971, *AJ*, **76**, 544
- Martell S. L., et al., 2021, *MNRAS*, **505**, 5340
- Montes D., Fernandez-Figueroa M. J., de Castro E., Cornide M., 1995, *A&AS*, **109**, 135
- Motch C., et al., 1998, *A&AS*, **132**, 341
- Moultaka J., Ilovaisky S. A., Prugniel P., Soubiran C., 2004, *PASP*, **116**, 693
- Norton A. J., et al., 2007, *A&A*, **467**, 785
- Pallavicini R., Randich S., Giampapa M. S., 1992, *A&A*, **253**, 185
- Pecaut M. J., Mamajek E. E., 2013, *ApJS*, **208**, 9
- Pojmanski G., 2002, *Acta Astron.*, **52**, 397
- Pye J. P., et al., 1995, *MNRAS*, **274**, 1165
- Randich S., 2009, in Mamajek E. E., Soderblom D. R., Wyse R. F. G., eds, Vol. 258, *The Ages of Stars*. pp 133–140, doi:10.1017/S1743921309031780
- Randich S., Gratton R., Pallavicini R., 1993, *A&A*, **273**, 194
- Randich S., Giampapa M. S., Pallavicini R., 1994, *A&A*, **283**, 893
- Ricker G. R., et al., 2015, *Journal of Astronomical Telescopes, Instruments, and Methods*, **1**, 014003
- Robb R. M., Vincent J., Thanjavur K., 2003, *Information Bulletin on Variable Stars*, **5449**, 1
- Roberts D. H., Lehar J., Dreher J. W., 1987, *AJ*, **93**, 968
- Ryan S. G., 1989, *AJ*, **98**, 1693
- Scargle J. D., 1982, *ApJ*, **263**, 835
- Smiljanic R., et al., 2018, *A&A*, **617**, A4
- Soubiran C., Le Campion J. F., Cayrel de Strobel G., Caillo A., 2010, *A&A*, **515**, A111
- Strassmeier K. G., Weber M., Granzer T., Järvinen S., 2012, *Astronomische Nachrichten*, **333**, 663
- Tonry J., Davis M., 1979, *AJ*, **84**, 1511
- Traulsen I., et al., 2019, *A&A*, **624**, A77
- Voges W., et al., 1999, *A&A*, **349**, 389
- Watson C. L., Henden A. A., Price A., 2006, *Society for Astronomical Sciences Annual Symposium*, **25**, 47
- Zahn J. P., 1989, *A&A*, **220**, 112
- Zickgraf F. J., Engels D., Hagen H. J., Reimers D., Voges W., 2003, *A&A*, **406**, 535

Table A1. Heliocentric radial velocities of the two components of TYC 3386-868-1.

HJD (2 450 000+)	RV _P (km s ⁻¹)	σ _{RV_P}	RV _S (km s ⁻¹)	σ _{RV_S}	Instrument
4459.7215	2.34	1.50	53.24	0.61	SARG
7331.6297	-39.75	0.69	88.40	0.58	CAOS
7336.5926	58.62	1.43	-11.84	0.84	CAOS
<i>9152.6506</i>	<i>22.35</i>	<i>6.62</i>	<i>22.35</i>	<i>6.62</i>	CAOS
9153.6690	-3.64	0.36	51.35	0.47	CAOS
9154.6183	-23.57	0.27	74.60	0.31	CAOS
9211.4989	-35.42	0.84	90.80	0.45	CAOS
9212.4992	-29.48	0.99	82.79	0.51	CAOS
9241.4697	-4.61	2.32	54.96	1.55	CAOS
<i>9242.4122</i>	<i>23.16</i>	<i>1.64</i>	<i>23.16</i>	<i>1.64</i>	CAOS
9250.4128	-1.27	3.42	52.76	2.05	CAOS
9251.3775	-21.33	0.89	74.95	0.52	CAOS
<i>9263.3402</i>	<i>23.80</i>	<i>0.47</i>	<i>23.80</i>	<i>0.47</i>	CAOS
9271.3725	56.50	1.84	-10.86	1.15	CAOS
9272.3788	78.70	1.97	-29.85	1.04	CAOS

Notes. RVs obtained close to the conjunctions are the same for the primary and secondary component and are written in italic.

Table A2. Heliocentric radial velocities of the two components of G 137-52.

HJD (2 450 000+)	RV _P (km s ⁻¹)	σ _{RV_P}	RV _S (km s ⁻¹)	σ _{RV_S}	Instrument
2439.3928	57.43	1.29	-10.19	1.48	AURELIE
2441.3860	-7.34	1.43	54.13	1.36	AURELIE
6749.6221	37.42	0.13	7.79	0.29	CAOS
6805.4164	46.08	0.16	-2.18	0.28	CAOS
6818.3565	-9.41	0.11	56.40	0.21	CAOS
6819.4305	3.11	0.11	41.73	0.19	CAOS
6839.3265	-4.75	0.10	52.41	0.19	CAOS
6845.4400	34.35	0.25	11.23	0.40	CAOS
6846.3591	56.45	0.11	-12.39	0.20	CAOS
7204.3486	49.24	0.12	-5.73	0.23	CAOS
7262.2984	-2.08	0.13	50.05	0.24	CAOS
7263.3128	-6.80	0.12	53.78	0.22	CAOS
7892.5272	30.57	0.20	14.61	0.39	CAOS
7897.4103	36.94	0.13	8.45	0.24	CAOS
7919.4674	-9.35	0.14	56.24	0.23	CAOS
<i>7920.4305</i>	<i>22.68</i>	<i>0.05</i>	<i>22.68</i>	<i>0.05</i>	CAOS
7934.4536	-11.01	0.12	58.19	0.19	CAOS
7941.4088	49.82	0.12	-4.96	0.19	CAOS

Notes. RVs obtained close to the conjunctions are the same for the primary and secondary component and are written in italic.

APPENDIX A: TABLES WITH INDIVIDUAL VALUES OF RADIAL VELOCITY

Table A3. Heliocentric radial velocities of the two components of BD+10 2953.

HJD (2 450 000+)	RV _P (km s ⁻¹)	σ _{RV_P}	RV _S (km s ⁻¹)	σ _{RV_S}	Instrument
4148.6430	-50.91	0.80	-15.19	0.92	SARG
6729.6474	-53.57	0.09	-16.48	0.20	CAOS
6734.6523	-42.17	1.82	-31.85	1.80	CAOS
6776.5294	-22.06	0.09	-50.40	0.20	CAOS
6818.4420	-4.51	0.10	-71.42	0.20	CAOS
6820.4257	-26.89	0.14	-48.72	0.25	CAOS
6845.4724	-18.15	0.04	-57.53	0.06	CAOS
6846.4040	-15.59	0.10	-60.02	0.20	CAOS
6852.3726	-8.46	0.12	-70.88	0.21	CAOS
7178.5403	-23.14	1.00	-51.75	0.94	CAOS
<i>7223.3655</i>	<i>-35.82</i>	<i>0.06</i>	<i>-35.82</i>	<i>0.06</i>	CAOS
7263.2980	-60.76	0.17	-8.72	0.26	CAOS
7568.4804	-53.22	0.10	-20.10	0.19	CAOS
7892.5101	-14.11	0.11	-61.11	0.20	CAOS
7897.3957	-67.88	0.10	-1.51	0.20	CAOS
7919.3978	-14.17	0.10	-59.83	0.19	CAOS
7920.3761	-11.70	0.10	-63.26	0.17	CAOS
7933.4627	-61.61	0.10	-6.81	0.18	CAOS
7941.4877	-41.82	0.76	-29.85	1.19	CAOS
<i>8262.4422</i>	<i>-35.52</i>	<i>0.05</i>	<i>-35.52</i>	<i>0.05</i>	CAOS
8277.4141	-39.84	0.40	-32.33	0.61	CAOS
8290.4077	-7.73	0.10	-66.55	0.19	CAOS
8299.4042	-68.25	0.11	-1.93	0.19	CAOS
8305.4078	-52.87	0.13	-16.38	0.30	CAOS
<i>8312.3615</i>	<i>-38.00</i>	<i>0.05</i>	<i>-38.00</i>	<i>0.05</i>	CAOS
9300.5913	-14.47	0.26	-59.43	0.25	CAOS

Notes. RVs obtained close to the conjunctions are the same for the primary and secondary component and are written in italic.

Table A4. Heliocentric radial velocities of the two components of V1079 Her.

HJD (2 450 000+)	RV _P (km s ⁻¹)	σ _{RV_P}	RV _S (km s ⁻¹)	σ _{RV_S}	Instrument
2439.4846	17.91	1.57	-45.20	1.38	AURELIE
2441.5015	41.48	1.52	-69.37	1.31	AURELIE
2443.3980	40.14	1.40	-69.29	1.30	AURELIE
6776.5673	-40.38	0.28	9.18	0.51	CAOS
6818.5406	-74.12	0.21	42.66	0.38	CAOS
6839.4504	-68.94	0.64	36.57	1.23	CAOS
6845.5206	23.98	0.31	-54.71	0.43	CAOS
6846.4786	34.78	0.41	-67.58	0.51	CAOS
6852.3969	-4.24	3.94	-23.04	2.59	CAOS
8262.5936	27.25	0.20	-58.17	0.37	CAOS
8277.4454	-49.05	0.18	17.99	0.29	CAOS
8291.4044	-55.76	0.20	21.52	0.34	CAOS
8299.4344	-5.57	0.26	-26.37	0.53	CAOS
8311.4260	-64.69	0.21	29.02	0.36	CAOS
8319.4545	5.23	0.27	-40.88	0.55	CAOS
8330.3594	-58.57	0.22	22.48	0.34	CAOS

Table A5. Heliocentric radial velocities of the two components of BD+62 1880.

HJD (2 450 000+)	RV _P (km s ⁻¹)	σ _{RV_P}	RV _S (km s ⁻¹)	σ _{RV_S}	Instrument
7261.5032	31.50	0.22	-77.29	0.79	CAOS
7263.4735	-53.11	0.21	38.93	0.76	CAOS
7308.3951	-82.11	0.18	80.32	0.66	CAOS
7336.4194	38.35	0.17	-86.03	0.61	CAOS
7599.5556	-38.61	0.16	20.06	0.53	CAOS
8306.5822	13.35	0.19	-59.15	0.72	CAOS
8311.5974	25.09	0.15	-72.08	0.54	CAOS
8312.5622	-68.60	0.18	62.09	0.66	CAOS
8330.5611	23.23	0.20	-71.17	0.82	CAOS
8367.4383	34.56	0.18	-78.81	0.71	CAOS
9154.2913	-77.93	0.22	75.53	0.59	CAOS
9446.4844	-79.72	0.53	75.82	0.99	CAOS
9453.4881	-60.65	0.70	55.32	0.98	CAOS
9454.4461	-59.39	0.63	50.90	1.15	CAOS
9455.4301	37.36	0.54	-86.94	0.90	CAOS
9459.4709	52.30	0.89	-101.16	1.21	CAOS
9467.4351	50.87	0.72	-96.84	1.14	CAOS

Table A6. Heliocentric radial velocities of the two components of TYC 4279-1821-1.

HJD (2 450 000+)	RV _P (km s ⁻¹)	σ _{RV_P}	RV _S (km s ⁻¹)	σ _{RV_S}	Instrument
2230.3281	33.13	1.49	-53.17	1.53	AURELIE
2234.3389	-19.19	1.59	4.75	1.80	AURELIE
7262.5687	-47.94	0.15	35.93	0.25	CAOS
7331.5103	30.93	0.14	-54.42	0.20	CAOS
7336.4839	-19.95	0.15	4.35	0.27	CAOS
9152.3811	30.50	0.16	-54.15	0.22	CAOS
9152.4050	30.22	0.20	-53.72	0.24	CAOS
9154.4664	10.63	0.23	-32.32	0.37	CAOS
9223.3211	-43.73	2.36	28.54	1.86	CAOS
9242.2367	5.95	2.45	-25.30	1.65	CAOS
9250.2387	-26.04	1.12	11.04	1.02	CAOS
9251.2569	-39.48	0.59	26.42	0.48	CAOS
9453.5268	-39.84	0.36	28.24	0.31	CAOS